INORGANIC CHEMISTRY FRONTIERS

RESEARCH ARTICLE

View Article Online
View Journal | View Issue



Cite this: *Inorg. Chem. Front.*, 2022, **9**, 4232



# Organic–inorganic hybrid phosphite-participating S-shaped penta-$Ce^{III}$-incorporated tellurotungstate as an electrochemical enzymatic hydrogen peroxide sensor for β-D-glucose detection†

Nizi Song, Yanzhou Li,* Yanying Wang, Menglu Wang, Mengling Liu, Lijuan Chen* and Junwei Zhao *

Received 15th April 2022,
Accepted 22nd June 2022

DOI: 10.1039/d2qi00816e

rsc.li/frontiers-inorganic

Polyoxometalate chemistry has made rapid advances in innovative structural chemistry. The lower valence state and lone electron pair effect of the subgroup-valence heteroatom Te(IV) can be introduced into tungsten–oxygen systems to construct complicated tellurotungstate (TT) aggregates. Thus, for the first time, we synthesized a phosphite-participating S-shaped penta-$Ce^{III}$-incorporated tetrameric TT aggregate, $Na_4K_3H_6[Ce_5W_4(Hpica)_6H_2P_2O_{12}(H_2O)_4]\{[B\text{-}\beta\text{-}TeW_7O_{28}]_2[B\text{-}\beta\text{-}TeW_8O_{30}]_2\}\cdot 94H_2O$ (**1**) (Hpica = 2-picolinic acid). The molecular structure of **1** consists of one tetrameric $[Ce_5W_4(Hpica)_6H_2P_2O_{12}(H_2O)_4]\{[B\text{-}\beta\text{-}TeW_7O_{28}]_2[B\text{-}\beta\text{-}TeW_8O_{30}]_2\}^{13-}$ (**1a**) hybrid polyanion constructed from two symmetrical sandwich-like $\{[Ce_2W_2(Hpica)_3\ HP^{III}O_6(H_2O)_2][B\text{-}\beta\text{-}TeW_7O_{28}][B\text{-}\beta\text{-}TeW_8O_{30}]\}^{8-}$ (**$\{Ce_2W_2P^{III}Te_2\}$**) moieties linked by a $Ce^{3+}$ cation. Interestingly, the sandwich-like **$\{Ce_2W_2P^{III}Te_2\}$** moiety can be viewed as a heterometal cluster $[Ce_2W_2(Hpica)_3HP^{III}O_6(H_2O)_2]^{10+}$ **$\{Ce_2W_2P^{III}\}$** group integrating a tetravacant $[B\text{-}\beta\text{-}TeW_8O_{30}]^{8-}$ fragment and a pentavacant $[B\text{-}\beta\text{-}TeW_7O_{28}]^{10-}$ fragment. Furthermore, **1** was converted into **nano-1** with the help of ultrasonication in organic solution. **Nano-1** was then complexed with $NH_2$-graphene (**$NH_2$-G**), and a bi-component **nano-1/$NH_2$-G** nanocomposite was prepared. Without further assembly and modification, the as-prepared **nano-1/$NH_2$-G** nanocomposite was first used as a sensor to detect hydrogen peroxide. This **nano-1/$NH_2$-G**-based $H_2O_2$ sensor shows excellent reproducibility, stability, and anti-interference ability. In quick succession, with the assistance of glucose oxide, an electrochemical enzymatic method based on the **nano-1/$NH_2$-G**-based $H_2O_2$ sensor was developed and further applied for the specific detection of β-D-glucose. This enzymatic sensor also displays good detection performance. The present work provides new insight into electrochemical sensors based on the **nano-1/$NH_2$-G** nanocomposite and their potential application in enzymatic glucose sensing.

## Introduction

The development of synthetic strategies has promoted important advances in the design of complex cluster architectures such as polyoxometalates (POMs).[1–8] These metal–oxygen clusters with unmatched physical and chemical properties not only represent a tremendous range of crystalline inorganic clusters but also have been employed as fundamental building blocks to construct novel gigantic cluster-based functional materials with special electronic characteristics,[9–12] nano-sized structures,[13–16] and unique photoelectric or magnetic properties.[17–21]

In the realm of POMs, heteropolyoxotungstates (HPOTs) are of great importance due to their high structural stability, diverse vacant building blocks and multiple application potentials, and have been extensively used and systematically explored for novel structural design purposes and application considerations.[22–25] Due to the lower valence state and lone electron pair effect of the subgroup-valence heteroatom Te(IV) with a triangular pyramidal coordination configuration, it has come to be considered an important member to generate lacunary HPOTs, known as tellurotungstates (TTs), which can be further employed to capture lanthanide (Ln) ions to fabricate high-nuclearity Ln-incorporated TTs (HNLITTs). The introduction of the Te(IV) heteroatom can enhance the feasibility of

*Henan Key Laboratory of Polyoxometalate Chemistry, College of Chemistry and Chemical Engineering, Henan University, Kaifeng 475004, China.
E-mail: 1079126956@qq.com, ljchen@henu.edu.cn, zhaojunwei@henu.edu.cn*

†Electronic supplementary information (ESI) available: Experimental details, PXRD, IR, TG curves, related structure and property figures and tables. Crystallographic information for **1**. CCDC 2163291 (**1**). For ESI and crystallographic data in CIF or other electronic format see DOI: https://doi.org/10.1039/d2qi00816e

obtaining excellent HNLITTs with amazing structural features. For instance, an outstanding octameric HNLITT $[\{(TeO_3)W_{10}O_{34}\}_8\{Ce_8(H_2O)_{20}\}(WO_2)_4(W_4O_{12})]^{48-}$ (Fig. S1a†) was obtained through a versatile one-step approach by Su's group,[26] which was constructed by eight $\{(TeO_3)W_9Ce\}$ segments and other bridging $\{WO_6\}$ groups. Later, they also reported a larger HNLITT, $[Ce_{10}Te_8W_{88}O_{298}(OH)_{12}(H_2O)_{40}]^{18-}$ (Fig. S1b†), which is different from the former and consists of two triangle $\{W_2O_5Ce(H_2O)_7\}$ linking units and two $[Te_4W_{42}O_{144}(OH)_6Ce_4(H_2O)_{13}]^{14-}$ fragments.[27] Three years later, Hu *et al.* reported a tetrameric HNLITT, $[\{Ln(H_2O)_5(TeW_{18}O_{64})\}_4]^{44-}$ (Ln = $Eu^{3+}$, $Gd^{3+}$) (Fig. S1c†), as the first HNLITT containing four Dawson-type building blocks.[28] Importantly, TT segments can also function as good inorganic mono- or polydentate ligands to combine with Ln cations in the participation of N/O-included organic components to construct organic–inorganic hybrid HNLITTs (OIHHNLITTs). At present, OIHHNLITTs, as an important branch of HNLITTs, are gradually becoming a research hotpot due to their diverse components, eye-catching topologies and broad application prospects. For example, in 2017, a series of Hpica-decorated tetrameric OIHHNLITTs, $[Ln_2(H_2O)_4(pica)_2W_2O_5][(Ln(H_2O)W_2(Hpica)_2O_4)(B\text{-}\beta\text{-}TeW_8O_{30}H_2)_2]^{24-}$ (Ln = $La^{3+}$, $Ce^{3+}$, $Nd^{3+}$, $Sm^{3+}$, and $Eu^{3+}$) (Fig. S1d†), was isolated by our group,[29] which is made up of two Ln–W-heterometal sandwiched $[(Ln(H_2O)W_2(Hpica)_2O_4)(B\text{-}\beta\text{-}TeW_8O_{30}H_2)_2]^{5-}$ moieties linked *via* one $\{Ln_2(H_2O)_4(pica)_2W_2O_5\}^{6+}$ cluster. Later, the introduction of the flexible ligand gluconic acid into the system led to the formation of a multi-D-gluconic-acid-bridging OIHHNLITT $[Eu_4(H_2O)_4W_6(H_2glu)_4O_{12}(B\text{-}\alpha\text{-}TeW_9O_{33})_4]^{24-}$ (Fig. S1e†), which is the first polyhydroxycarboxylic-bridging HNLITT.[30] This tetrameric polyanion can be viewed as the aggregation of an innovative $[Eu_4(H_2O)_4W_6(H_2glu)_4O_{12}]^{8+}$ core and four $[B\text{-}\alpha\text{-}TeW_9O_{33}]^{8-}$ fragments. These studies open the door to the design of new-type OIHHNLITTs with amazing structure features. However, all the above-mentioned OIHHNLITTs are almost totally made up of the trivacant $[TeW_9O_{33}]^{8-}$ building blocks, limiting structural innovation and breakthrough in the design of novel structures.

To further break the bottleneck in the development of the above-mentioned OIHHNLITTs, another phosphite $[HPO_3]^{2-}$ anion was chosen to introduce in the reaction system. Because the phosphite anion is composed of one H and three O atoms, it presents an approximate tetrahedral geometry. Although coexisting triangular pyramidal $TeO_3^{2-}$ and tetrahedral $HPO_3^{2-}$ groups in the reaction system may be competitive, they also open up more possibilities for reactions and construction of structures. If the tetrahedral $[HPO_3]^{2-}$ anion can be incorporated into OIHHNLITTs, it will be conducive to introduce more Ln ions in these structures, which greatly enriches the types of OIHHNLITT structures and promotes the innovation and sustainable development of HPOTs. Based on these ideas, an Hpica-functionalized phosphite-participating S-shaped HNLITT, $Na_4K_3H_6[Ce_5W_4(Hpica)_6H_2P_2O_{12}(H_2O)_4]\{[B\text{-}\beta\text{-}TeW_7O_{28}]_2[B\text{-}\beta\text{-}TeW_8O_{30}]_2\}\cdot 94H_2O$ (**1**), was synthesized. It is noteworthy that the $[HPO_3]^{2-}$ anionic units in this structure act as bridging functional groups, connecting two $Ce^{3+}$ cations and two pentavacant $[B\text{-}\beta\text{-}TeW_7O_{28}]^{10-}$ segments. Furthermore, **1** was further prepared as **nano-1** with the aid of ultrasonication in organic solution. Moreover, **nano-1** was further modified with $NH_2$-graphene (**$NH_2$-G**), resulting in the formation of a bi-component **nano-1/$NH_2$-G** nano-composite. Subsequently, the as-prepared **nano-1/$NH_2$-G** nano-composite was used as a sensor for the detection of hydrogen peroxide. Furthermore, with the assistance of glucose oxidase (GOD), an electrochemical enzymatic sensor was created based on the **nano-1/$NH_2$-G**-based $H_2O_2$ sensor for the specific detection of β-D-glucose in $NaH_2PO_4$–$Na_2HPO_4$ phosphate buffer (pH = 6.5). The present work provides new insight into electrochemical sensors based on the **nano-1/$NH_2$-G** nanocomposite and their potential application in enzymatic GOD sensing.

## Results and discussion

### Synthesis of 1

$Na_2WO_4\cdot 2H_2O$ (3.402 g, 10.314 mmol), dimethylamine hydrochloride (0.701 g, 8.601 mmol), $K_2TeO_3$ (0.130 g, 0.512 mmol) and $H_3PO_3$ (5.000 mL, 0.01 g $mL^{-1}$) were dissolved in distilled water (20 mL). The pH value was adjusted to 5 using 6 M HCl. The solution was heated to 60 °C for 30 min. $Ce(NO_3)_3\cdot 6H_2O$ (0.402 g, 0.923 mmol) and Hpica (0.201 g, 1.203 mmol) were consecutively added to the solution and the final pH of the solution was kept at 5 using 4.0 M NaOH. The solution was heated at 90 °C for 2 h, cooled and filtered. Slow evaporation led to yellow block crystals after about one week. Yield: 11.8% (based on $K_2TeO_3$). Elemental analysis (calcd %): C, 3.68 (3.52); H, 1.68 (1.92); N, 0.65 (0.68); P, 0.47 (0.50); Na, 0.66 (0.75); K, 0.86 (0.95); Ce, 6.0 (5.70); Te, 4.26 (4.15); W, 51.20 (50.85). In the synthetic process, the effects of the amount (0.691, 0.923, 1.152, and 1.382 mmol) of $Ce(NO_3)_3\cdot 6H_2O$ and pH value (2.00, 3.00, 4.00, 5.00, and 6.00) on the crystal growth were explored. Firstly, with an increase in the $Ce(NO_3)_3\cdot 6H_2O$ dosage from 0.691 mmol to 0.923 mmol, the growth rate of the crystals was accelerated, but an amorphous precipitate was formed when the $Ce(NO_3)_3\cdot 6H_2O$ dosage was greater than 0.923 mmol. The best-quality crystals were obtained when the $Ce(NO_3)_3\cdot 6H_2O$ dosage was 0.923 mmol. Moreover, when the pH was 2 or 6, an amorphous precipitate was produced. **1** was isolated in the pH range of 3–5. However, when the pH was 3 or 4, crystals of **1** were formed, accompanied by some precipitate. When the pH was 5, only crystals of **1** were obtained and no precipitate was observed. Therefore, the optimum pH is 5 for crystal growth of **1**.

### Structural description

**1** belongs to the monoclinic space group *C*2/*c* (Table S1†), where the results were also certified by IR spectroscopy (Fig. S2†) and PXRD (Fig. S3†). Its structure consists of a novel $[Ce_5W_4(Hpica)_6H_2P_2O_{12}(H_2O)_4]\{[B\text{-}\beta\text{-}TeW_7O_{28}]_2[B\text{-}\beta\text{-}TeW_8O_{30}]_2\}^{13-}$ (**1a**) hybrid polyanion (Fig. 1a), four $Na^+$, three $K^+$, six $H^+$ and eighteen crystal water molecules. The S-shaped **1a** anion can

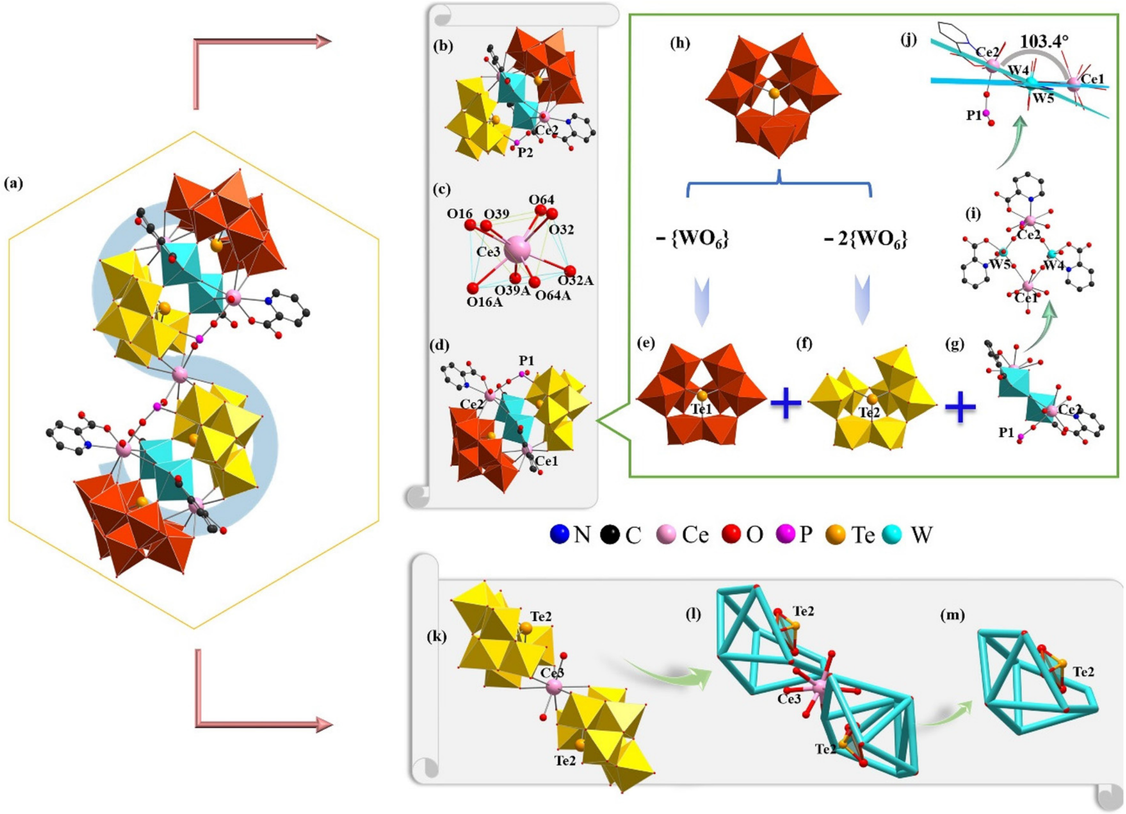


**Fig. 1** (a) S-shaped **1a** anion. (b and d) Sandwich-like **{$Ce_2W_2P^{III}Te_2$}** moiety. (c) Coordination environment of $Ce3^{3+}$. (e) Tetravacant [B-β-$TeW_8O_{30}$]$^{8-}$ subunit. (f) Pentavacant [B-β-$TeW_7O_{28}$]$^{10-}$ subunit. (g) The **{$Ce_2W_2P^{III}$}** cluster. (h) Trivacant [B-β-$TeW_9O_{33}$]$^{8-}$ fragment. (i) Twisted parallelogram formed by Ce1, Ce2, W4 and W5 atoms. (j) The surface defined by W4, W5, $Ce1^{3+}$ and $Ce2^{3+}$ atoms. (k) The 1 : 2 type {Ce3[B-β-Te2$W_7O_{28}$]$_2$}$^{17-}$ fragment. (l) Simplified view of the 1 : 2 type {Ce3[B-β-Te2$W_7O_{28}$]$_2$}$^{17-}$ fragment. (m) Simplified view of the pentavacant [B-β-$TeW_7O_{28}$]$^{10-}$ subunit. Color code: W, turquoise; Te, light orange; O, red; P, pink; Ce, rose; C, black; N, blue; {$TeW_8$}, brick red; {$TeW_7$}, gold.

be further viewed as two sandwich-like {[$Ce_2W_2$(Hpica)$_3$ $HP^{III}O_6(H_2O)_2$][B-β-$TeW_7O_{28}$][B-β-$TeW_8O_{30}$]}$^{8-}$ (**{$Ce_2W_2P^{III}Te_2$}**) (Fig. 1b and d) moieties linked by a $Ce3^{3+}$ cation. The $Ce3^{3+}$ ion located at the symmetrical center exhibits a twisted square antiprism (Fig. 1c), where four coordination oxygen atoms (O16, O32, O39, and O64) on the same plane come from the [B-β-$TeW_7O_{28}$]$^{10-}$ subunit [Ce3–O16: 2.500 Å, Ce3–O32: 2.447 Å, Ce3–O39: 2.480 Å and Ce3–O64: 2.415 Å]. Furthermore, the sandwich-like **{$Ce_2W_2P^{III}Te_2$}** moiety could be deemed as one tetralacunary [B-β-Te1$W_8O_{30}$]$^{8-}$ (Fig. 1e) subunit and a pentalacunary [B-β-Te2$W_7O_{28}$]$^{10-}$ (Fig. 1f) subunit connected by a heterometallic [$Ce_2W_2$(Hpica)$_3HP^{III}O_6(H_2O)_2$]$^{10+}$ **{$Ce_2W_2P^{III}$}** (Fig. 1g) cluster. The [B-β-Te1$W_8O_{30}$]$^{8-}$ (Fig. 1e) subunit stems from the [B-β-Te1$W_9O_{33}$]$^{8-}$ fragment (Fig. 1h) by losing a {$WO_6$} octahedron in the {$W_3O_{13}$} trimetallic cluster. Similarly, the [B-β-Te2$W_7O_{28}$]$^{11-}$ (Fig. 1f) subunit can be regarded as being obtained by the trivacant [B-β-Te2$W_9O_{33}$]$^{8-}$ (Fig. 1h) fragment, losing two {$WO_6$} octahedra in two different trimetallic clusters, one of which is the rotated 60° trimetallic cluster, resulting from the α configuration to the β configuration, whereas the other is a trimetallic cluster that links to another trimetallic cluster through a corner-sharing motif. In the **{$Ce_2W_2P^{III}$}** cluster, a twisted quadrilateral is formed by Ce1, Ce2, W4 and W5 atoms through four bridging oxygen atoms (Fig. 1i). The dihedral angle between the surface formed by the Ce1, W4, and W5 atoms and the surface defined by the Ce2, W4, and W5 atoms is 103.4° (Fig. 1j). From another point of view, **1a** can be considered as a combination of two [B-β-Te1$W_8O_{30}$]$^{8-}$ (Fig. 1e) subunits, two heterometallic **{$Ce_2W_2P^{III}$}** (Fig. 1g) clusters and a 1 : 2-type {Ce3[B-β-Te2$W_7O_{28}$]$_2$}$^{17-}$ fragment (Fig. 1k). This 1 : 2-type {Ce3[B-β-Te2$W_7O_{28}$]$_2$}$^{17-}$ fragment can be further simplified to the simple snippets (Fig. 1l), and the half of the simple snippet (Fig. 1l) can be seen as a bowl formed by oxygen atoms on the edge of the pentavacant Keggin [B-β-$TeW_7O_{28}$]$^{10-}$ subunit (Fig. 1m). It is worth mentioning that three 2-Hpica ligands adopt two different coordination environments in the **{$Ce_2W_2P^{III}$}** cluster (Fig. 2a). However, there is no 2-Hpica ligand in the $Ce1^{3+}$ cation. The $Ce1^{3+}$ cation occupies the eight-coordinate distorted square antiprism established by one water ligand (O1W), three O (O11, O17 and O44) atoms from the tetravacant [B-β-Te1$W_8O_{30}$]$^{8-}$ segment and two O atoms (O4 and O14) from the pentavacant [B-β-Te2$W_7O_{28}$]$^{10-}$ segment, and one $\mu_2$-O7 atom and one $\mu_2$-O21 atom (Fig. 2b). The $Ce2^{3+}$ cation also adopts a distorted square antiprism geometry (Fig. 2c), in

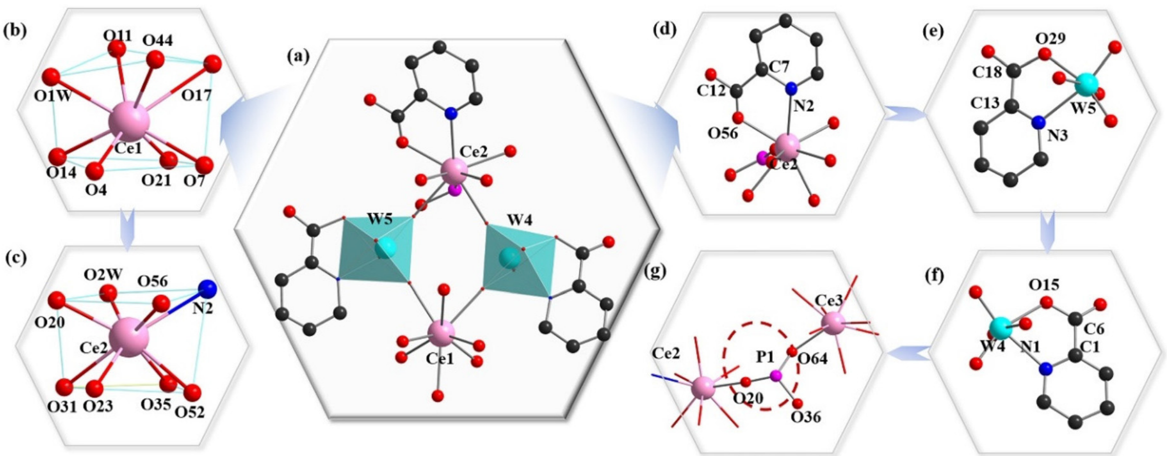


**Fig. 2** (a) The $[Ce_2W_2(Hpica)_3O_4(H_2O)_2]^{10+}$ connectome. (b and c) Square antiprism geometries of $Ce1^{3+}$ and $Ce2^{3+}$ ions. (d–f) Coordination environments of the $Ce2^{3+}$, W5 and W4 centers, respectively. (g) Connection of the $\{HP^{III}O_3\}$ group and $Ce2^{3+}$ and $Ce3^{3+}$ ions. Color codes: W, turquoise; Te, light orange; O, red; P, pink; Ce, rose; C, black; N, blue; $\{TeW_8\}$, brick red; $\{TeW_7\}$, gold.

which the N2 and O56 atoms are from the same 2-Hpica ligand and $\mu_2$-O20 is from the $\{HP^{III}O_3\}$ group (Fig. 2d). The remaining coordination atoms are O2 W, $\mu_2$-O23, $\mu_2$-O31, O35 and O52, respectively, where the O35 and O52 atoms are from the tetravacant $[B\text{-}\beta\text{-}Te1W_8O_{30}]^{8-}$ subunit. The other two 2-Hpica ligands coordinate with the W4 and W5 atoms *via* a carboxyl oxygen atom and a pyridine nitrogen atom, respectively, producing two five-membered rings, [W5–O29–C18–C13–N3 (Fig. 2e) and W4–O15–C6–C1–N1 (Fig. 2f)].

The W4 and W5 atoms display the octahedral configuration (Fig. 2a). This coordination mode and type of 2-Hpica greatly improve the stability of **1a**. It is surprising that the tetrahedral $\{HP^{III}O_3\}$ group (Fig. 2g) (this proton is omitted) links $Ce2^{3+}$, $Ce3^{3+}$ and $[B\text{-}\beta\text{-}TeW_7O_{28}]^{10-}$. The tetrameric **1a** is the first example of a phosphite-participating OIHHNLITT. This type of HNLITT with high-vacancy mixed building TT blocks is very rare in the system of POM structures, which may be related to the higher pH synthetic conditions and offers a new idea for preparing HPOT-based materials in the future.

To maintain charge balance and enhance the structural stability of **1a**, some charge compensation ions ($Na^+$ and $K^+$) and lattice water molecules are required, which interact with **1a** through electrostatic and H-bond interactions to give birth to the 3-D supramolecular architecture. To better comprehend the stacking motifs, each **1a** anion is simplified as two diagonally connected triangles along the *a*, *b* and *c* axes (Fig. 3a–h). In the *bc* plane (Fig. 3a–d), the tetrameric **1a** anions present the –ABAB– stacking pattern. To easily observe the stacking pattern of **1a** anions, it was split into layers A (Fig. 3b) and B (Fig. 3c). The simplification of the –ABAB– stacking mode of **1a** anions is further shown in Fig. 4d on the *bc* plane. From the perspective of the *b* axis (Fig. 3e and f), the **1a** anions are distributed in an –AAA– fashion, while the Ce atoms of each **1a** anions are arranged in an Arabic number “8” pattern (Fig. 3f). Additionally, in the *ab* plane (Fig. 3g and h), the **1a** anions present a more complex stacking pattern. Specifically, the **1a** anions are placed in an –ABAB– pattern along the *a* axis and in the –ABCD– stacking pattern along the *b* axis. However, a special stacking mode is formed among adjacent **1a** anions. Each **1a** anion is surrounded by three polyanions. Through this staggered mode, every six **1a** anions form a lantern-shaped hexagon (Fig. 3h). In addition, it is worth mentioning that **1** shows high stability up to 300 °C in an $N_2$ atmosphere (Fig. S4†), which provides a foundation for its further application and functionalization.

## Design strategy and characterization of nano-1 and nano-1/NH2-G composite

The crystal structure of **nano-1** obtained by ultrasonication is consistent with that of **1**, which can be confirmed by the good agreement of the IR spectra (Fig. S2†) and PXRD patterns (Fig. S3†) of **1** and **nano-1**. The process for the fabrication of the **nano-1/$NH_2$-G** composite is schematically represented in Scheme 1a–c. As is known, the introduction of an active substrate possessing a high-specific surface area and electroconductibility is a useful method to promote the electrochemical application of POM-based materials.[31,32] **$NH_2$-G** is an ideal conductive substrate due to its low cost, high electrical conductivity, amino-functionalized surface and huge surface area. Also, **$NH_2$-G** possesses abundant active sites to combine with POMs based on supramolecular interactions and electrostatic attraction. Thus, **$NH_2$-G** acts as a conductive substrate. Alternatively, nano-POMs can work as functional precursors to produce composite materials owing to the exposure of the abundant active sites of nanosized POMs with stable morphologies.[33,34] Here, **nano-1** was utilized as a precursor to composite with **$NH_2$-G** to prepare the **nano-1/$NH_2$-G** composite. The above-mentioned preparation strategy has the advantages of **$NH_2$-G** and nano-POMs, compensating for the disadvantage of the single species and adapting to the requirements of electrochemical sensors. Considering the superior properties and prospective potential of nanosized POMs,

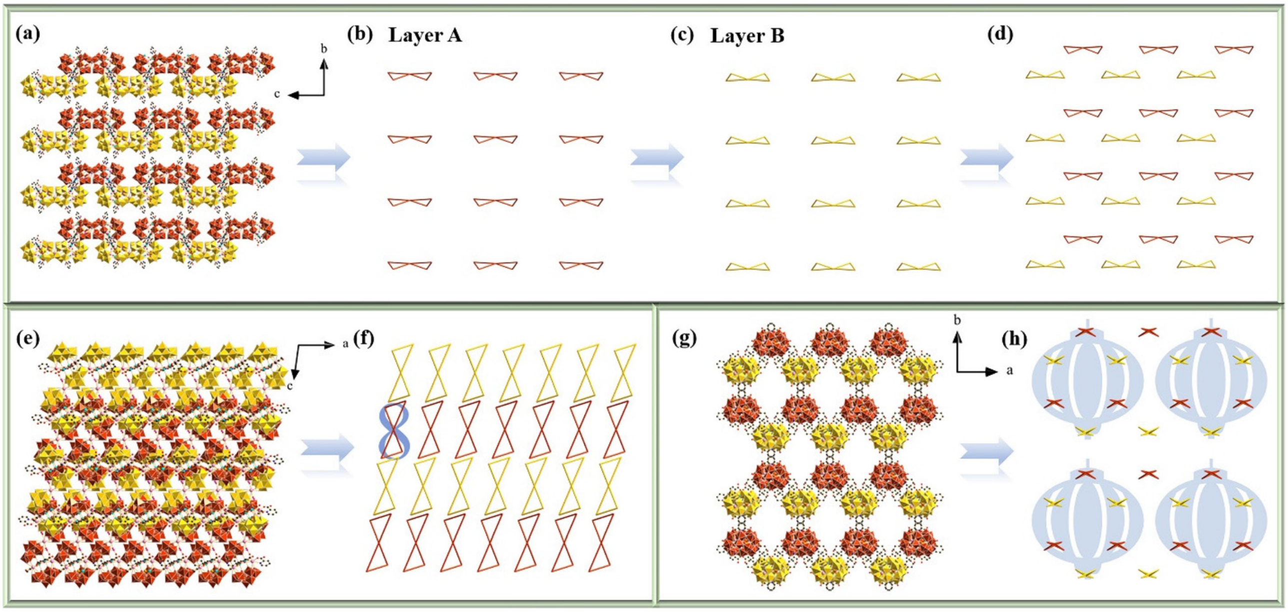


Fig. 3 (a) 3D stacking of **1a** anions in the *bc* plane. (b and c) Simplified layer A and layer B, displaying two spatial orientations of **1a** anions in the *bc* plane. (d) Simplified stacking of **1a** anions in the *bc* plane. (e and f) 3D stacking and simplified stacking of **1a** anions in the *ac* plane. (g and h) 3D stacking and simplified stacking of **1a** anions in the *ab* plane.

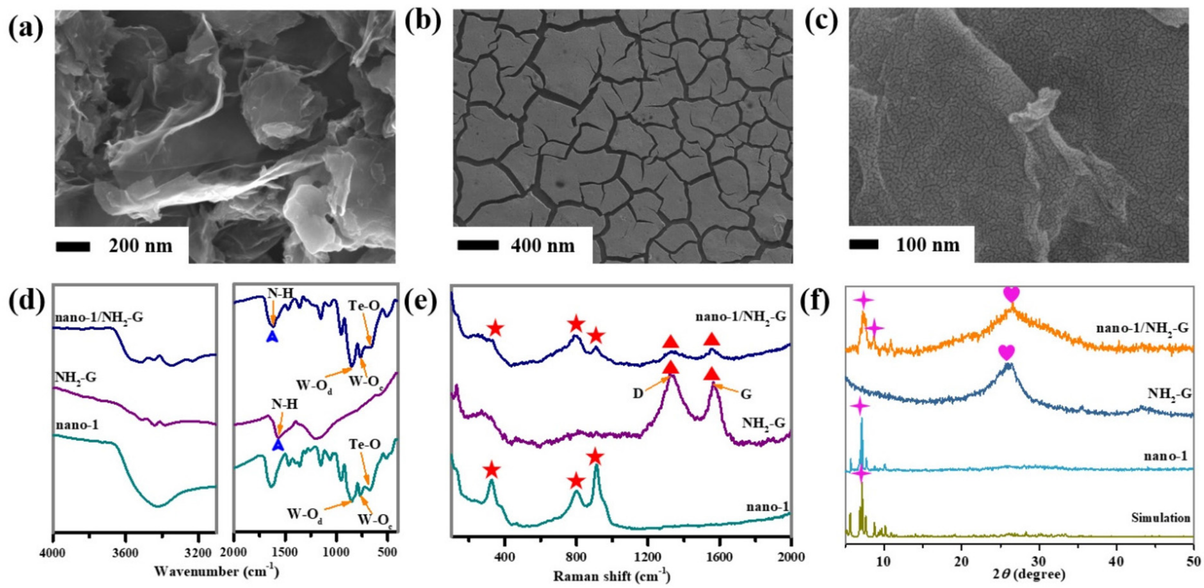


Fig. 4 (a–c) SEM images of **$NH_2$-G**, **nano-1** and **nano-1/$NH_2$-G**. (d) IR spectra, (e) Raman spectra and (f) PXRD patterns of simulation of **1**, **nano-1**, **$NH_2$-G**, and **nano-1/$NH_2$-G**.

**nano-1** was prepared with the help of ultrasonication in EtOH solution. The UV reflection spectrum (Fig. S5†) of **nano-1** was applied to obtain its optical bandgap (2.88 eV) using the Tauc plot method, which proved that it is an optical semiconductor. Specifically, the effective combination of semiconductor **nano-1** and highly electrically conductive **$NH_2$-G** can facilitate electron transfer and improve the sensing performance of the **nano-1/$NH_2$-G** composite. To find the optimal proportion of **nano-1/$NH_2$-G**, **nano-1/$NH_2$-G** composites with proportions of 0.5 : 1, 1 : 1, 1.5 : 1, 2 : 1 and 2.5 : 1 were prepared and their successful preparation was also proved by IR spectra (Fig. S6a†) and PXRD patterns (Fig. S6b†). Through CV measurements (Fig. S7†) of **nano-1/$NH_2$-G** modified glassy carbon electrodes (**GCEs**) with different proportions of **nano-1/$NH_2$-G** in 0.1 M PBS (pH = 6.5) with 6.0 mM $H_2O_2$, it could be distinctly found that the CV peak current of **nano-1/$NH_2$-G-GCE** is the strongest

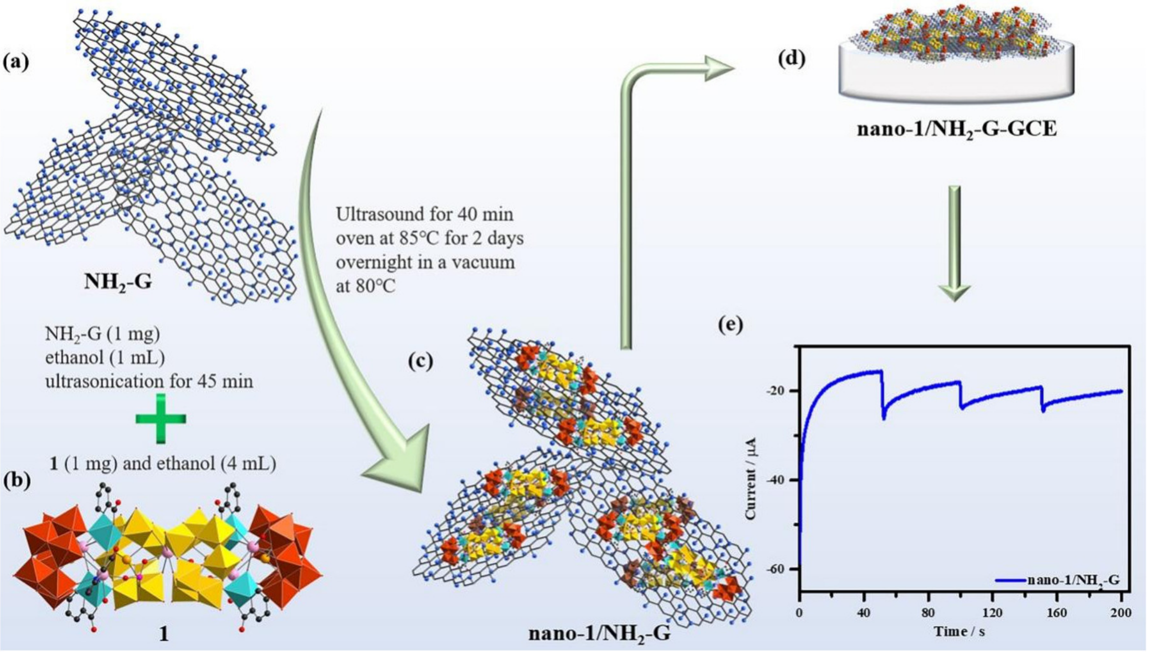


**Scheme 1** Schematic preparation process of **nano-1/NH$_2$-G-GCE**. (a) Schematic structure of **NH$_2$-G**. (b) Crystal structure of **1**. (c) Schematic structure of **nano-1/NH$_2$-G**. (d) The **nano-1/NH$_2$-G-GCE**. (e) Schematic detection curve.

when the proportion of **nano-1/NH$_2$-G** is 1 : 1. Therefore, the optimal proportion of **nano-1/NH$_2$-G** was determined to be 1 : 1. Furthermore, SEM was used to characterize the morphologies of the as-synthesized materials (**NH$_2$-G : nano-1** = 1 : 1). Fig. 4a illustrates the leaflike nanosheet morphology of **NH$_2$-G** with a smooth surface. The morphology of **nano-1** shows a cracked film (Fig. 4b), presenting the successful construction of the **nano-1** film, which was strongly supported by SEM-EDS elemental mapping analysis (Fig. S8†). The **nano-1/NH$_2$-G** nanomorphology is exhibited in Fig. 4c, in which the smooth surface of **NH$_2$-G** is fully covered by the cracked film of **nano-1**, verifying the successfully preparation of the **nano-1/NH$_2$-G** composite. It is obvious that the ultrathin nanosheet morphology of **NH$_2$-G** was maintained, which acts as the soft highly electrically conducting support of **nano-1**.

To confirm the structures of all the nanosized samples, the IR spectra, Raman spectra and PXRD patterns of **nano-1**, **NH$_2$-G** and **nano-1/NH$_2$-G** were measured. The functional groups of **nano-1**, **NH$_2$-G** and **nano-1/NH$_2$-G** were observed in their FT-IR spectra (Fig. 4d). Three groups of characteristic peaks at 852, 759 and 667 cm$^{-1}$ were observed for **nano-1**, which correspond to the $\nu$(W–O$_d$), $\nu$(W–O$_c$) and $\nu$(Te–O$_a$) stretching vibrations, respectively. In the spectrum of **NH$_2$-G**, the intensity of the signals at 3437 and 1571 cm$^{-1}$ was greatly reduced. The signal at 1571 cm$^{-1}$ is attributed to the N–H bond. These observations indicate the successful preparation of **nano-1/NH$_2$-G**.[35] Furthermore, as revealed in Fig. 4e, the characteristic Raman peaks for **nano-1** were observed at 324 (W–O), 793 (Te–O), 920 (W–O) and 966 (P–O) cm$^{-1}$ (Fig. S9†), whereas the main Raman peaks for **NH$_2$-G** were seen at 1328 and 1568 cm$^{-1}$, which are consistent with that in the literature.[36] For **nano-1/NH$_2$-G**, its Raman peaks (330, 791, 915, 1330, and 1563 cm$^{-1}$) are very similar to that of each of its component. Moreover, the crystalline structures of **nano-1**, **NH$_2$-G** and **nano-1/NH$_2$-G** were further characterized by PXRD tests (Fig. 4f). For **nano-1**, its PXRD peaks match well with its single-crystal XRD mode (Fig. S2†). The PXRD peaks of **NH$_2$-G** match that in the literature.[36] For **nano-1/NH$_2$-G**, its PXRD peaks are made up of that of **nano-1** and **NH$_2$-G**. In addition, all the samples showed good crystallinity. Meanwhile, the elemental composition of

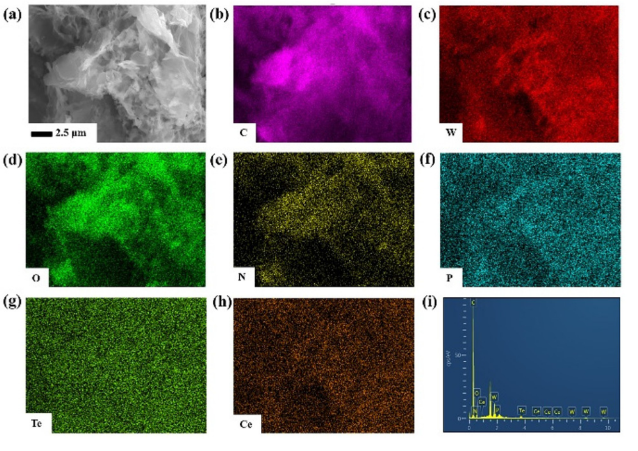


**Fig. 5** (a) SEM image of **nano-1/NH$_2$-G** at the 2.5 μm scale. (b–h) SEM-EDS C, W, O, N, P, Te and Ce elemental mapping images of **nano-1/NH$_2$-G** on a silicon substrate. (i) EDS of **nano-1/NH$_2$-G**.

**nano-1/NH$_2$-G** was investigated by SEM-EDS mapping measurements. As shown in Fig. 5, the SEM-EDS elemental mapping data of **nano-1/NH$_2$-G** confirm the existence and a homogeneous distribution of C (Fig. 5b), W (Fig. 5c), O (Fig. 5d), N (Fig. 5e), P (Fig. 5f), Te (Fig. 5g) and Ce (Fig. 5h) elements, further verifying the successful composition of **nano-1** and **NH$_2$-G**.

## Electrochemical properties of the nano-1/NH2-G-based biosensor

$H_2O_2$ is closely involved in many important physiological and biochemical reactions in organisms.[37,38] $H_2O_2$ is produced to mediate a variety of physiological responses, including cell proliferation, differentiation and migration. In addition, $H_2O_2$ also plays an important role in food processing, disinfection and drug production.[39,40] In the dairy industry, $H_2O_2$ is widely used as a preservative to prevent spoilage of dairy products and extend their shelf life.[41] However, excessive $H_2O_2$ can lead to neurodegenerative diseases, cancer, diabetes and other health problems.[42,43] Therefore, the accurate measurement of the $H_2O_2$ concentration is very important. The traditional methods for the determination of $H_2O_2$ include colorimetry, fluorescence, flow injection and electrochemical luminescence.[44,45] However, the applications of these methods are limited by their complex and time-consuming procedures and expensive equipment. Hence, the development of economical, efficient and sensitive methods for the detection of $H_2O_2$ is vital. According to the literature,[46–48] the electrochemical method has the advantages of quick response, simple operation, high sensitivity and good selectivity.

POMs can be used as an electronic container that can receive or lose one or more electrons.[49] This, the application of the catalytic activity and biocompatibility of POMs in electrochemical sensing has aroused the interest of researchers. Previously, some investigations on POM-based sensors have been reported for the electrochemical sensing of myricetin,[50] clenbuterol and ractopamine,[51] cholesterol,[52] dopamine[34] and uric acid.[53] At present, in the related research on electrochemical sensors, the introduction of carbon nanomaterials in POM systems endows them with some better electrochemical performances such as improved stability and reproducibility, a wider detection range, lower detection limit and good selectivity.[54] Among the carbon materials, **NH$_2$-G** bearing good electroconductibility and biocompatibility can accelerate electron transfer to improve the signal intensity. Also, the positively charged **NH$_2$-G** can be combined with the negatively charged POMs by electrostatic attractions. Based on these considerations, the **nano-1/NH$_2$-G** composite was utilized to modify **GCE** (Scheme 1d and e) for further electrochemically detecting $H_2O_2$.

Fig. 6a depicts the cyclic voltammetry (CV) curves of **GCE** (dotted line), **NH$_2$-G-GCE** (dash line) and **nano-1/NH$_2$-G-GCE** (solid line) in 0.1 M PBS (pH = 6.5) in the presence (navy blue) or absence (pink) of 6.0 mM $H_2O_2$ (scan rate 100 mV $s^{-1}$) in the potential window of −0.5–0.6 V. Apparently, when $H_2O_2$ was present, only **nano-1/NH$_2$-G-GCE** showed a dramatic increase in current response at about −0.3 V, which is derived

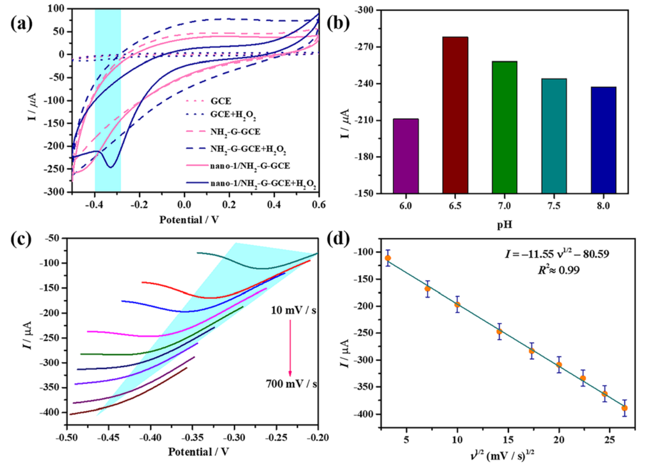


Fig. 6 (a) CV curves of **GCE**, **NH$_2$-G-GCE** and **nano-1/NH$_2$-G-GCE** in 0.1 M PBS (pH = 6.5) with 6.0 mM $H_2O_2$. (b) Evolution of cathode peak current derived from W centers in **nano-1** with pH for **nano-1/NH$_2$-G-GCE** in 0.1 M PBS (pH = 6.5) with 6.0 mM $H_2O_2$. (c) CV curves of **nano-1/NH$_2$-G-GCE** in 0.1 M PBS (pH = 6.5) with 6.0 mM $H_2O_2$ at various scan rates. (d) Plot of cathode peak current derived from the W centers in **nano-1** *vs.* the square root of the scan rate.

from the reduction procedure of tungsten atoms in **nano-1**, indicating the effective electrocatalytic reduction of $H_2O_2$ by **nano-1/NH$_2$-G-GCE**. This observation indicates that **nano-1/NH$_2$-G-GCE** could immensely enhance the electroconductibility and catalytic capability by rapid electron transfer. In contrast, the bare **GCE** did not display a variation in current intensity in the presence or absence of $H_2O_2$, demonstrating almost no electrocatalytic reduction activity for $H_2O_2$.

Afterwards, to explore the optimum $H_2O_2$ detection conditions, CV measurements of **nano-1/NH$_2$-G-GCE** under different pH values in 0.1 M PBS with 6.0 mM $H_2O_2$ (scan rate 100 mV $s^{-1}$) were performed (Fig. 6b and Fig. S10†). The results indicate that the catalytic activity was affected by pH. The optimal pH was found to be 6.5. In addition, the CV curves of **nano-1/NH$_2$-G-GCE** under various scan rates were also studied. The influence of scan rate ($\nu$) on the electrocatalytic reduction of $H_2O_2$ was evaluated in the range of 10–700 mV $s^{-1}$ (Fig. 6c and Fig. S11†). It is glaringly obvious that the cathode peak current is proportional to the square root of the scan rate, which is fitted using the equation $I = -11.55\ (\nu)^{1/2} - 80.59$ ($R^2$ = 0.99) (Fig. 6d). This phenomenon manifests that the electrochemical interface reaction between **nano-1/NH$_2$-G-GCE** and solution is a diffusion-controlled process.[55]

A suitable working potential is crucial for the electrochemical detection of $H_2O_2$. This is because a too low working potential will decrease the sensitivity of the sensor to effectively detect $H_2O_2$. As presented in Fig. 7a, the amperometric response curves (ARCs) were measured under different working potentials in 0.1 M PBS (pH = 6.5) with 6.0 mM $H_2O_2$, which indicate that the response current gradually decreased when the potential increased in the range of −0.30–0 V. Obviously, the maximum response current appeared at the

 

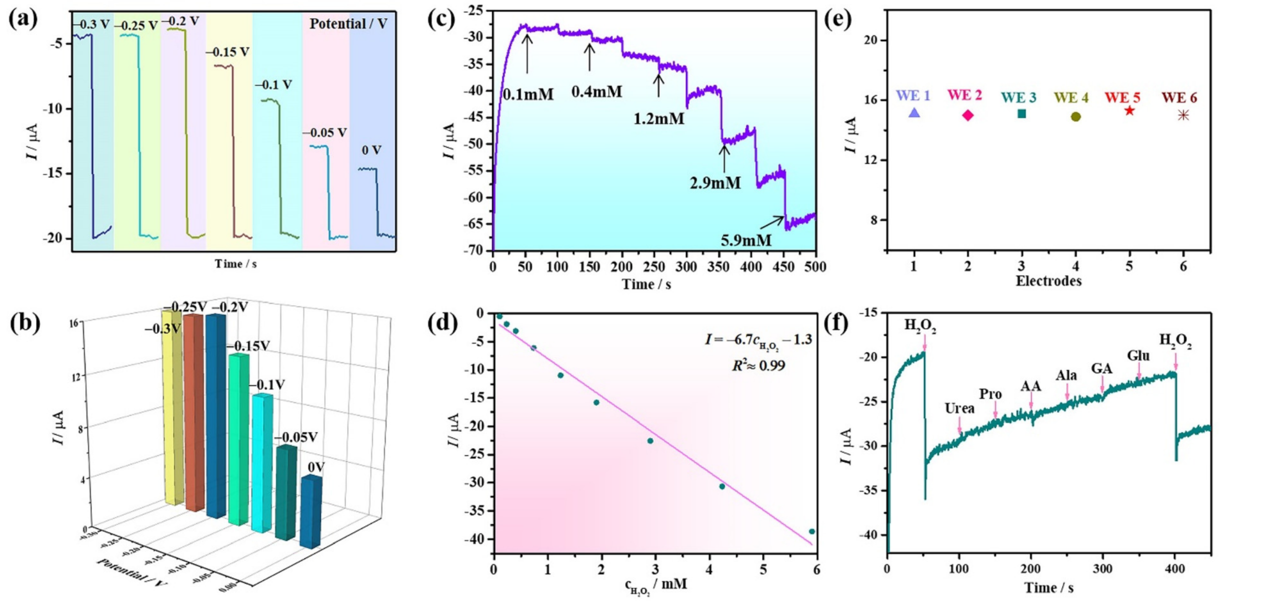

Fig. 7 (a) ARCs of **nano-1/NH$_2$-G-GCE** under different applied potentials in 0.1 M PBS (pH = 6.5) with 6.0 mM $H_2O_2$. (b) Comparison of amperometric responses (*I*) at different potentials to obtain the optimal applied potential. (c) ARC of **nano-1/NH$_2$-G-GCE** with the successive addition of diverse concentrations of $H_2O_2$ in 0.1 M PBS (pH = 6.5) at −0.20 V. (d) Plot of *I vs.* $c_{H_2O_2}$. (e) Comparison of peak currents of six independent **nano-1/NH$_2$-G-GCEs** in 0.1 M PBS (pH = 6.5) with 6.0 mM $H_2O_2$ at −0.20 V. (f) ARC of **nano-1/NH$_2$-G-GCE** in 0.1 M PBS (pH = 6.5) with the successive addition of 1.0 mM of $H_2O_2$ and 1.0 mM interferents (urea, Pro, AA, Ala, GA, and glu) in 0.1 M PBS (pH = 6.5) at −0.20 V.

potential of −0.20 V, and consequently −0.20 V was chosen as the best potential for the detection of $H_2O_2$. Consequently, the potential of −0.20 V was applied for testing the ARCs of **nano-1/NH$_2$-G-GCE** by successively adding $H_2O_2$ to 0.1 M PBS (pH = 6.5). To exclude the effect of the baseline current under different applied potentials, the amperometric current response values under different potentials are provided in Fig. 7b, further confirming that the optimal potential is −0.20 V. To quantitatively probe the determination property of **nano-1/NH$_2$-G-GCE**, the amperometric current response changes were recorded with the continuous addition of different concentrations of $H_2O_2$ (0.1–5.9 mM) to 0.1 M PBS (pH = 6.5) at −0.2 V (Fig. 7c). A noteworthy variation in the response current was observed after each addition of $H_2O_2$. When the concentration of $H_2O_2$ was less than 5.9 mM, **nano-1/NH$_2$-G-GCE** generated a rapid response signal, revealing that **nano-1/NH$_2$-G-GCE** has high sensitivity for the detection of $H_2O_2$ in the range of 0.1–5.9 mM. Fig. 7d reveals the plot of the response current *versus* $H_2O_2$ concentration (0.1–5.9 mM), which obeys the function $I = -6.7c_{H_2O_2} - 1.3$ with a correlation coefficient of 0.99. The reproducibility of the as-prepared **nano-1/NH$_2$-G-GCE** as an $H_2O_2$ sensor was also tested. Herein, six independent **nano-1/NH$_2$-G-GCEs** were tested in 0.1 M PBS (pH = 6.5) solution with 6.0 mM $H_2O_2$ at −0.20 V (Fig. 7e). Their relative standard deviation (RSD) was 1.2%, demonstrating the outstanding reproducibility of **nano-1/NH$_2$-G-GCEs** for the detection of $H_2O_2$. These results demonstrate that **nano-1/NH$_2$-G-GCE** is a good electrochemical sensor for the detection of $H_2O_2$, which may be derived from the synergistic effect of **nano-1** and **NH$_2$-G**.

Furthermore, antijamming capability, reproducibility and stability are vital parameters affecting the sensing properties. The antijamming capability immediately influences the precision of recognition. Some interferents in the real environment readily generate interference signals in the detection of $H_2O_2$. Hence, several common interferents such as urea, proline (Pro), ascorbic acid (AA), glucose (Glu), alanine (Ala) and gluconic acid (GA) were selected to evaluate the antijamming capability of **nano-1/NH$_2$-G-GCE**. Fig. 7f shows ARC of **nano-1/NH$_2$-G-GCE** after the successive addition of 1.0 mM urea, 1.0 mM Pro, 1.0 mM AA, 1.0 mM Ala, 1.0 mM GA, 1.0 mM Glu, and 1.0 mM $H_2O_2$ in 0.1 M PBS (pH = 6.5). Obviously, the addition of urea, Pro, AA, Ala, GA, and Glu produced a negligible current response compared to $H_2O_2$, manifesting the preeminent anti-interference ability and selectivity for **nano-1/NH$_2$-G-GCE** in the detection of $H_2O_2$. In addition, a time-dependent stability test on **nano-1/NH$_2$-G-GCE** was also carried out. After one week of storage at 4 °C, the current response of **nano-1/NH$_2$-G-GCE** still maintained 93% of the initial value (Fig. S12†), illustrating its good time-dependent stability.

## Electrochemical glucose detection based on nano-1/NH$_2$-G-GCE $H_2O_2$ biosensor

Although the first enzyme electrode was invented in 1962,[56] much more endeavours have been dedicated to enhancing blood glucose monitoring techniques in the past five decades. Most commercial glucose monitors utilize the enzyme-based electrochemical method. GOD is a commonly used enzyme, which can specifically catalyze β-D-glucose (β-D-Glu) under aerobic conditions. The optimum working temperature of GOD is 0–30 °C and the best pH is 5.5–6.5.[57] The optimum pH of **nano-1/NH$_2$-G-GCE** in this work is also in this range. Therefore, an enzyme electrochemical glucose sensing system was designed (Fig. 8). 10 mg GOD, 0.1 g β-D-Glu and 10 mg GOD + 0.1 g β-D-Glu were added to 2.0 mL PBS (0.1 M, pH 6.5), respectively, and incubated at 30 °C for 30 min. Then, 100 μL of these solutions were injected into 15.0 mL PBS (0.1 M, pH = 6.5), respectively, and their current response measured. As illustrated in Fig. 8, the **nano-1/NH$_2$-G-GCE** biosensor showed little or no significant amperometric current response for only the presence of GOD or β-D-Glu in 0.1 M PBS (pH = 6.5) at −0.2 V. In contrast, the GOD + β-D-Glu system for the **nano-1/NH$_2$-G-GCE** biosensor exhibited a significant amperometric current response. The enzyme-catalysed reaction is as follows:

$$\beta\text{-D-Glu} + \text{oxygen} + H_2O + \text{GOD} \rightarrow \text{gluconic acid} + H_2O_2.$$

Thus, with the help of GOD, β-D-Glu can be detected by detecting $H_2O_2$ using our **nano-1/NH$_2$-G-GCE** biosensor.[58] To explore the effect of heating time of β-D-Glu and GOD on the current response, we chose four time points to perform the experiments. As shown in Fig. 9, the heating time was the best at 30 min. After 30 min, the current response decreased slightly with an increase in time. This may be due to the decomposition of trace $H_2O_2$. Therefore, we chose the current response value to calculate the concentration of $H_2O_2$ produced by the reaction at a heating time of 30 min. Using the measured the current response value in the above-mentioned equation $I = -6.7c_{H_2O_2} - 1.3$ led to the concentration of produced $H_2O_2$ being 250.74 mM in the reaction system consisting of 10 mg GOD and 0.1 g β-D-Glu. This result reveals that 250.74 mM β-D-Glu was detected, while the actual added β-D-Glu concentration was 277.7 mM, and thus the relative error was 9.7%. Therefore, this electrochemical enzymatic method can effectively detect β-D-Glu.

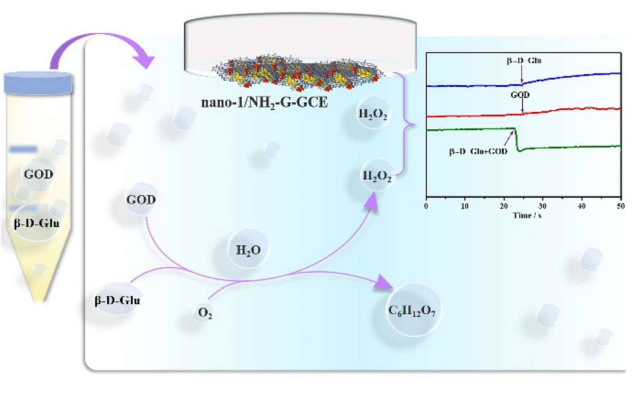


Fig. 8 Schematic enzyme electrochemical glucose sensing system and ARCs of the **nano-1/NH$_2$-G-GCE** sensor with the addition of β-D-Glu, GOD and β-D-Glu + GOD in 0.1 M PBS (pH = 6.5) at −0.20 V.

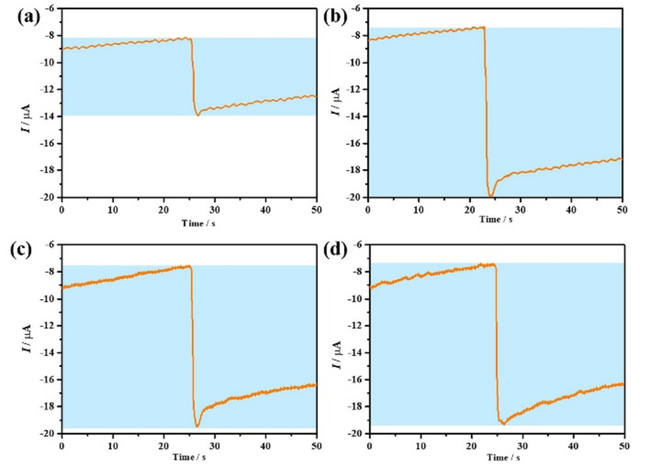


Fig. 9 (a–d) ARCs of **nano-1/NH$_2$-G-GCE** towards a β-D-Glu + GOD solution at heating times of 0, 30, 60 and 90 min, respectively. The tests were carried out in 0.1 M PBS (pH = 6.5) at −0.20 V.

## Conclusions

In conclusion, the introduction of the tetrahedral $[HPO_3]^{2-}$ anion in the OIHHNLITT system led to the formation of the fascinating Hpica-functionalized phosphite-participating S-shaped HNLITT **1**. This result indicates that the $[HPO_3]^{2-}$ anion can be used as an anion template to tune the structural assembly of HNLITTs, demonstrating a feasible synthetic route to generate new HPOTs with different types of heteroatoms. In addition, the **nano-1/NH$_2$-G** composite was successfully prepared using a simple method, which then was used to develop an electrochemical sensor platform for the detection of $H_2O_2$ and β-D-Glu, respectively. The electrochemical studies showed that this HNLITT may be a good candidate for developing promising electrochemical sensing applications.

## Author contributions

Nizi Song and Yanzhou Li performed syntheses, characterization, electrochemical properties and wrote the manuscript. Yanying Wang, Menglu Wang participated in PXRD, IR and TG characterization. Lijuan Chen and Junwei Zhao provided research ideas, determined crystal structures and revised all over the manuscript.

## Conflicts of interest

There are no conflicts to declare.

## Acknowledgements

This work was supported by the National Natural Science Foundation of China (21871077, 22071042, 22001058, 22171070, 21771052), the Program for Innovation Teams in

 

Science and Technology in Universities of Henan Province (20IRTSTHN004), and the Program of First-Class Discipline Cultivation Project of Henan University (2019YLZDYJ02, CJ1205A0240019).

## References


1 C. F. Li, K. Yamaguchi and K. Suzuki, Ligand-directed approach in polyoxometalate synthesis: formation of a new divacant lacunary polyoxomolybdate $[\gamma\text{-PMo}_{10}O_{36}]^{7-}$, *Angew. Chem., Int. Ed.*, 2021, **60**, 6960–6964.

2 L. L. Liu, J. Jiang, G. P. Liu, X. D. Jia, J. W. Zhao, L. J. Chen and P. Yang, Hexameric to trimeric lanthanide-included selenotungstates and their 2D honeycomb organic–-inorganic hybrid films used for detecting ochratoxin A, *ACS Appl. Mater. Interfaces*, 2021, **13**, 35997–36010.

3 Z. H. Pan, Z. Z. Weng, X. J. Kong, L. S. Long and L. S. Zheng, Lanthanide-containing clusters for catalytic water splitting and CO2 conversion, *Coord. Chem. Rev.*, 2022, **457**, 214419.

4 X. Chen, Z. Wang, R. Zhang, L. Xu and D. Sun, A novel polyoxometalate-based hybrid containing a 2D $[CoMo_8O_{26}]_\infty$ structure as the anode for lithium-ion batteries, *Chem. Commun.*, 2017, **53**, 10560–10563.

5 S. Omwoma, C. T. Gore, Y. C. Ji, C. W. Hu and Y. F. Song, Environmentally benign polyoxometalate materials, *Coord. Chem. Rev.*, 2015, **286**, 17–29.

6 X. F. Yi, N. V. Lzarova, M. Stuckart, D. Guerin, L. Thomas, S. Lenfant, D. Vuillaume, J. V. Leusen, T. Duchoň, S. Nemšák, S. D. M. Bourone, S. Schmitz and P. Kögerler, Probing frontier orbital energies of $\{Co_9(P_2W_{15})_3\}$ polyoxometalate clusters at molecule-metal and molecule-water interfaces, *J. Am. Chem. Soc.*, 2017, **139**, 14501–14510.

7 T. Wang, T. Ji, W. L. Chen, X. H. Li, W. Guan, Y. Geng, X. L. Wang, Y. G. Li and Z. H. Kang, Polyoxometalate film simultaneously converts multiple low-value all-weather environmental energy to electricity, *Nano Energy*, 2020, **68**, 104349.

8 A. Bijelic, A. Manuel and A. Rompel, Polyoxometalates as potential next-generation metallodrugs in the combat against cancer, *Angew. Chem., Int. Ed.*, 2019, **58**, 2980–2999.

9 S. R. Li, H. Y. Wang, H. F. Su, H. J. Chen, M. H. Du, L. S. Long, X. J. Kong and L. S. Zheng, A giant 3d-4f polyoxometalate super-tetrahedron with high proton conductivity, *Small Methods*, 2021, **5**, 2000777.

10 B. Huang, D. H. Yang and B. H. Han, Application of polyoxometalate derivatives in rechargeable batteries, *J. Mater. Chem. A*, 2020, **8**, 4593–4628.

11 L. B. Ni, G. Yang, Y. Liu, Z. Wu, Z. Y. Ma, C. Shen, Z. X. Lv, Q. Wang, X. X. Gong, J. Xie, G. W. Diao and Y. G. Wei, Self-assembled polyoxometalate nanodots as bidirectional cluster catalysts for polysulfide/sulfide redox conversion in lithium-sulfur batteries, *ACS Nano*, 2021, **15**, 12222–12236.

12 L. Y. Wu, L. Y. Guo, H. F. Su, M. Jagodič, M. Luo, X. Q. Zhou, S. Y. Zeng, C. H. Tung, D. Sun and L. S. Zheng, Two unprecedented POM-based inorganic-organic hybrids with concomitant heteropolytungstate and molybdate, *Inorg. Chem.*, 2017, **56**, 2481–2489.

13 S. J. Li, Y. Zhao, S. Knoll, R. J. Liu, G. Li, Q. P. Peng, P. T. Qiu, D. F. He, C. Streb and X. N. Chen, High proton-conductivity in covalently Linked polyoxometalate organoboronic acid-polymers, *Angew. Chem., Int. Ed.*, 2021, **60**, 16953–16957.

14 L.-Y. Guo, M. Jagodič, S.-Y. Zeng, Z. Wang, Z.-Q. Shi, X.-P. Wang, C.-H. Tung and D. Sun, pH-Controlled assembly of two novel Dawson-sandwiched clusters involving the in situ reorganization of trivacant $\alpha\text{-}[P_2W_{15}O_{56}]^{12-}$ into divacant $\alpha\text{-}[P_2W_{16}O_{57}]^{8-}$, *Dalton Trans.*, 2016, **45**, 8404–8411.

15 J. C. Liu, J. F. Wang, Q. Han, P. Shangguan, L. L. Liu, L. J. Chen, J. W. Zhao, C. Streb and Y. F. Song, Multicomponent self-assembly of a giant heterometallic polyoxotungstate supercluster with antitumor activity, *Angew. Chem., Int. Ed.*, 2021, **60**, 11153–11157.

16 S. S. Zhang, J. Y. Chen, K. Li, J. D. Yuan, H. F. Su, Z. Wang, M. Kurmoo, Y. Z. Li, Z. Y. Gao, C. H. Tung, D. Sun and L. S. Zheng, Janus cluster: asymmetric coverage of a $Ag^{43}$ cluster on the symmetric Preyssler P5W30 polyoxometalate, *Chem. Mater.*, 2021, **33**, 9708–9714.

17 K. Yang, Y. Y. Hu, L. Y. Li, L. L. Cui, L. He, S. J. Wang, J. W. Zhao and Y. F. Song, First high-nuclearity mixed-valence polyoxometalate with hierarchical interconnected Zn2+ migration channels as an advanced cathode material in aqueous zinc-ion battery, *Nano Energy*, 2020, **74**, 104851.

18 C. Zou, Z. J. Zhang, X. Xu, Q. H. Gong, J. Li and C. D. Wu, A multifunctional organic-inorganic hybrid structure based on MnIII-porphyrin and polyoxometalate as a highly effective dye scavenger and heterogenous catalyst, *J. Am. Chem. Soc.*, 2012, **134**, 87–90.

19 W. J. Luo, J. Hu, H. L. Diao, B. Schwarz, C. Streb and Y. F. Song, Robust polyoxometalate/nickel foam composite electrodes for sustained electrochemical oxygen evolution at high pH, *Angew. Chem., Int. Ed.*, 2017, **56**, 4941–4944.

20 S. Y. Lai, K. H. Ng, C. K. Cheng, H. Nur, M. Nurhadi and M. Arumugam, Photocatalytic remediation of organic waste over Keggin-based polyoxometalate materials: A review, *Chemosphere*, 2021, **263**, 128244.

21 Y. J. Dong, Q. Han, Q. Y. Hu, C. J. Xu, C. Z. Dong, Y. Peng, Y. Ding and Y. Q. Lan, Carbon quantum dots enriching molecular nickel polyoxometalate over CdS semiconductor for photocatalytic water splitting, *Appl. Catal., B*, 2021, **293**, 120214.

22 S. T. Zheng, J. Zhang and G. Y. Yang, Designed synthesis of POM-organic frameworks from $\{Ni_6PW_9\}$ building blocks under hydrothermal conditions, *Angew. Chem., Int. Ed.*, 2008, **47**, 3909–3913.

23 D. Wang, J. Jiang, M. Y. Cao, S. S. Xie, Y. M. Li, L. J. Chen, J. W. Zhao and G. Y. Yang, An unprecedented dumbbell-shaped pentadeca-nuclear W–Er heterometal cluster stabilizing nanoscale hexameric arsenotungstate aggregate and

electrochemical sensing properties of its conductive hybrid film-modified electrode, *Nano Res.*, 2022, **15**, 3628–3637.

24 A. J. Surman, P. J. Robbins, J. Ujma, Q. Zheng, P. E. Barran and L. Cronin, Sizing and discovery of nanosized polyoxometalate clusters by mass spectrometry, *J. Am. Chem. Soc.*, 2016, **138**, 3824–3830.

25 K. Yonesato, S. Yamazoe, D. Yokogawa, K. Yamaguchi and K. Suzuki, A molecular hybrid of an atomically precise silver nanocluster and polyoxometalates for H2 cleavage into protons and electrons, *Angew. Chem., Int. Ed.*, 2021, **60**, 16994–16998.

26 W. C. Chen, H. L. Li, X. L. Wang, K. Z. Shao, Z. M. Su and E. B. Wang, Assembly of cerium(III)-stabilized polyoxotungstate nanoclusters with $SeO_3^{2-}$/$TeO_3^{2-}$ templates: from single polyoxoanions to inorganic hollow spheres in dilute solution, *Chem. – Eur. J.*, 2013, **19**, 11007–11015.

27 W. C. Chen, C. Qin, X. L. Wang, Y. G. Li, H. Y. Zang, K. Z. Shao, Z. M. Su and E. B. Wang, Assembly of a large Cerium(III)-containing tungstotellurites(IV) nanocluster: $[Ce_{10}Te_8W_{88}O_{298}(OH)_{12}(H_2O)_{40}]^{18-}$, *Dalton Trans.*, 2015, **44**, 11290–11293.

28 S. X. Shang, Z. G. Lin, A. X. Yin, S. Yang, Y. N. Chi, Y. Wang, J. Dong, B. Liu, N. Zhen, C. L. Hill and C. W. Hu, Self-Assembly of Ln(III)-containing tungstotellurates(VI): correlation of structure and photoluminescence, *Inorg. Chem.*, 2018, **57**, 8831–8840.

29 Q. Han, Y. Wen, J. C. Liu, W. Zhang, L. J. Chen and J. W. Zhao, Rare-earth-incorporated tellurotungstate hybrids functionalized by 2-picolinic acid ligands: syntheses, structures, and properties, *Inorg. Chem.*, 2017, **56**, 13228–13240.

30 Y. Zhang, D. Wang, B. X. Zeng, L. J. Chen, J. W. Zhao and G. Y. Yang, An unprecedented polyhydroxycarboxylic acid ligand bridged multi-$Eu^{III}$ incorporated tellurotungstate and its luminescence properties, *Dalton Trans.*, 2020, **49**, 8833–8948.

31 J. Jiang, L. L. Liu, G. P. Liu, D. Wang, Y. Zhang, L. J. Chen and J. W. Zhao, Organic-inorganic hybrid cerium-encapsulated selenotungstate including three building blocks and its electrochemical detection of dopamine and paracetamol, *Inorg. Chem.*, 2020, **59**, 15355–15364.

32 S. S. Xie, J. Jiang, D. Wang, Z. G. Tang, R. F. Mi, L. J. Chen and J. W. Zhao, Tricarboxylic-ligand-decorated lanthanoid-inserted heteropolyoxometalates built by mixed-heteroatom-directing polyoxotungstate units: syntheses, structures, and electrochemical sensing for 17β-estradiol, *Inorg. Chem.*, 2021, **60**, 7536–7544.

33 X. R. Li, H. G. Xue and H. Pang, Facile synthesis and shape evolution of well-defined phosphotungstic acid potassium nanocrystals as a highly efficient visible-light-driven photocatalyst, *Nanoscale*, 2017, **9**, 216–222.

34 B. X. Zeng, Y. Zhang, Y. H. Chen, G. P. Liu, Y. Z. Li, L. J. Chen and J. W. Zhao, 3-D antimonotungstate framework based on 2,6-H2pdca connecting iron-cerium heterometallic Krebs-type polyoxotungstates for detecting small biomolecules, *Inorg. Chem.*, 2021, **60**, 2663–2671.

35 J. Yu, Y. Y. Zhang, H. Li, Q. J. Wan, Y. W. Li and N. J. Yang, Electrochemical properties and sensing applications of nanocarbons: A comparative study, *Carbon*, 2018, **129**, 301–309.

36 R. Kumar, K. Jahan, R. Nagarale and A. Sharma, Nongassing long-lasting electroosmotic pump with polyanilinewrapped aminated graphene electrodes, *ACS Appl. Mater. Interfaces*, 2015, **7**, 593–601.

37 Y. Zhao, Z. Zhang, Z. Pan and Y. Liu, Advanced bioactive nanomaterials for biomedical applications, *Exploration*, 2021, **1**, 20210089.

38 Z. Wu, M. M. Liu, Z. C. Liu and Y. Tian, Real-time imaging and simultaneous quantification of mitochondrial $H_2O_2$ and ATP in neurons with a single two-photon fluorescence-lifetime-based probe, *J. Am. Chem. Soc.*, 2020, **142**, 7532–7541.

39 Y. Yang, Z. T. Zeng, G. M. Zeng, D. L. Huang, R. Xiao, C. Zhang, C. Y. Zhou, W. P. Xiong, W. J. Wang, M. Cheng, W. J. Xue, H. Guo, X. Tang and D. H. He, Ti3C2 mxene/porous γ-C3N4 interfacial Schottky junction for boosting spatial charge separation in photocatalytic $H_2O_2$ production, *Appl. Catal., B*, 2019, **258**, 117956.

40 C. Samanta, Direct synthesis of hydrogen peroxide from hydrogen and oxygen: An overview of recent developments in the process, *Appl. Catal., A*, 2008, **350**, 133–149.

41 M. Jose, C. Martin, G. B. Brieva and L. G. F. Jose, Hydrogen peroxide synthesis: An outlook beyond the anthraquinone process, *Angew. Chem., Int. Ed.*, 2006, **45**, 6962–6984.

42 J. X. Fan, M. Y. Peng, H. Wang, H. R. Zheng, Z. L. Liu, C. X. Li, X. N. Wang, X. H. Liu, S. X. Cheng and X. Z. Zhang, Engineered bacterial bioreactor for tumor therapy via fenton-like reaction with localized $H_2O_2$ generation, *Adv. Mater.*, 2019, **31**, 1808278.

43 Y. Zhang, H. Yang, D. Wei, X. Zhang, J. Wang, X. Wu and J. Chang, Mitochondria-targeted nanoparticles in treatment of neurodegenerative diseases, *Exploration*, 2021, **1**, 20210115.

44 Z. J. Zhang, Y. B. Liu, X. H. Zhang and J. W. Liu, A cell-mimicking structure converting analog volume changes to digital colorimetric output with molecular selectivity, *Nano Lett.*, 2017, **17**, 7926–7931.

45 L. Li, Z. Y. Xing, Q. R. Tang, L. Yang, L. Dai, H. Wang, T. Yan, W. Y. Xu, H. M. Ma and Q. Wei, Enzyme-free colorimetric immunoassay for protein biomarker enabled by loading and disassembly behaviors of polydopamine nanoparticles, *ACS Appl. Bio Mater.*, 2020, **3**, 8841–8848.

46 C. L. Huang, Y. Chai, Y. F. Jiang, J. Forth, P. D. Ashby, M. M. L. Arras, K. L. Hong, G. S. Smith, P. C. Yin and T. P. Russell, The interfacial assembly of polyoxometalate nanoparticle surfactants, *Nano Lett.*, 2018, **18**, 2525–2529.

47 E. B. Bahadır and M. K. Sezgintürk, Electrochemical biosensors for hormone analyses, *Biosens. Bioelectron.*, 2015, **68**, 62–71.

48 Z. H. Su, X. L. Xu, Y. B. Cheng, Y. M. Tan, L. T. Xiao, D. L. Tang, H. M. Jiang, X. L. Qin and H. X. Wang, Chemical pre-reduction and electro-reduction guided

 

preparation of a porous graphene bionanocomposite for indole-3-acetic acid detection, *Nanoscale*, 2019, **11**, 962–967.
49 D. F. Chaia, J. Carlos, G. Garcíab, B. Lia, H. J. Pang, H. Y. Ma, X. M. Wang and L. C. Tan, Polyoxometalate-based metal-organic frameworks for boosting electrochemical capacitor performance, *Chem. Eng. J.*, 2019, **373**, 587–597.
50 R. M. Xing, L. Y. Tong, X. Y. Zhao, H. L. Liu, P. T. Ma, J. W. Zhao, X. Q. Liu and S. H. Liu, Rapid and sensitive electrochemical detection of myricetin based on polyoxometalates/$SnO_2$/gold nanoparticles ternary nanocomposite film electrode, *Sens. Actuators, B*, 2019, **283**, 35–41.
51 L. H. Zhang, Q. W. Wang, Y. Qi, L. Li, S. T. Wang and X. H. Wang, An ultrasensitive sensor based on polyoxometalate and zirconium dioxide nanocomposites hybrids material for simultaneous detection of toxic clenbuterol and ractopamine, *Sens. Actuators, B*, 2019, **288**, 347–355.
52 N. Thakur, M. Kumar, S. D. Adhikary, D. Mandal and T. C. Nagaiah, PVIM–$Co_5$POM/MNC composite as a flexible electrode for the ultrasensitive and highly selective non-enzymatic electrochemical detection of cholesterol, *Chem. Commun.*, 2019, **55**, 5021–5024.
53 Z. Y. Bai, C. L. Zhou, H. B. Xu, G. L. Wang, H. J. Pang and H. Y. Ma, Polyoxometalates-doped Au nanoparticles and reduced graphene oxide: A new material for the detection of uric acid in urine, *Sens. Actuators, B*, 2017, **243**, 361–371.
54 Y. C. Ji, L. J. Huang, J. Hu, C. Streb and Y. F. Song, Polyoxometalate-functionalized nanocarbon materials for energy conversion, energy storage and sensor systems, *Energy Environ. Sci.*, 2015, **8**, 776–789.
55 M. H. Yang, S. B. Hong, J. H. Yoon, D. S. Kim, S. W. Jeong, D. E. T. Yoo, J. Lee, K. G. Lee, S. J. Lee and B. G. Choi, Fabrication of flexible, redoxable, and conductive nanopillar arrays with enhanced electrochemical performance, *ACS Appl. Mater. Interfaces*, 2016, **8**, 22220–22226.
56 L. C. Clark and C. Lyons, Electrode systems for continuous monitoring in cardiovascular surgery, *Ann. N. Y. Acad. Sci.*, 1962, **102**, 29–45.
57 A. Heller and J. Ulstrup, Detlev Müller's discovery of glucose oxidase in 1925, *Anal. Chem.*, 2021, **93**, 7148–7149.
58 X. G. Luo, J. Xia, X. Y. Jiang, M. R. Yang and S. L. Liu, Cellulose-Based strips designed based on a sensitive enzyme colorimetric assay for the low concentration of glucose detection, *Anal. Chem.*, 2019, **91**, 15461–15468.